

**1 Development of a blood oxygenation phantom for photoacoustic
2 tomography combined with online pO₂ detection and flow
3 spectrometry**

4 Marcel Gehrung^{a,b}, Sarah E. Bohndiek^{a,b}, Joanna Brunker^{a,b,*}

5 ^aCancer Research UK Cambridge Institute, Li Ka-Shing Centre, Cambridge, UK

6 ^bDepartment of Physics, University of Cambridge, Cambridge, UK

7 Abstract. Photoacoustic tomography (PAT) is intrinsically sensitive to blood oxygen saturation (sO_2) *in vivo*. However, making accurate sO_2 measurements without knowledge of tissue- and instrumentation-related correction factors is extremely challenging. We have developed a low-cost flow phantom to facilitate validation of photoacoustic tomography systems. The phantom is composed of a flow circuit of tubing partially embedded within a tissue mimicking material, with independent sensors providing online monitoring of the optical absorption spectrum and partial pressure of oxygen in the tube. We first test the flow phantom using two small molecule dyes that are frequently used for photoacoustic imaging: methylene blue (MB) and indocyanine green (ICG). We then demonstrate the potential of the phantom for evaluating sO_2 using chemical oxygenation and deoxygenation of blood in the circuit. Using this dynamic assessment of the photoacoustic sO_2 measurement in phantoms in relation to a ground truth, we explore the influence of multispectral processing and spectral coloring on accurate assessment of sO_2 . Future studies could exploit this low-cost dynamic flow phantom to validate fluence correction algorithms and explore additional blood parameters such as pH, and also absorptive and other properties of different fluids.

19 Keywords: blood oxygenation, flow, phantom, photoacoustic tomography.

20 *Joanna Brunker, jb2014@cam.ac.uk

21 1 Introduction

22 Photoacoustic tomography (PAT) exploits optically generated ultrasound to provide images that
23 combine the high contrast and spectral specificity of optical imaging with the high spatial reso-
24 lution of ultrasound. In particular, PAT has been widely used to image blood hemoglobin con-
25 centration and oxygenation, which have the potential to inform on a range of pathophysiologies,
26 from tumour aggressiveness¹ and treatment response^{2,3} to intestinal inflammation associated with
27 Crohn's disease⁴ and colitis.⁵ The derivation of such images is usually based on spectral unmixing
28 to resolve the differential absorption contributions of oxy- (HbO_2) and deoxy-hemoglobin (Hb).
29 Total hemoglobin concentration (THb) is typically taken as the sum of the contributions to the
30 photoacoustic signal $P(\mathbf{r}, \lambda)$ from HbO_2 and Hb, while hemoglobin oxygenation (sO_2) is taken as

31 the ratio of HbO_2 to THb.

32 Unfortunately, the assessment of HbO_2 and Hb content from photoacoustic data is not triv-
33 ial. Estimation of these chromophore concentrations from images taken at multiple wavelengths
34 is commonly achieved using least-squares fitting of reference HbO_2 and Hb spectra,⁶ which are
35 tabulated in the literature;^{7–9} however, these absorption spectra are recorded under *in vitro* condi-
36 tions thus can vary substantially from the the attenuation spectra (incorporating both absorption
37 and scattering) experienced within an *in vivo* study. Moreover, the measured photoacoustic signal
38 $P(\mathbf{r}, \lambda)$ is not directly proportional to the absorbed energy density $H(\mathbf{r}, \lambda)$. $H(\mathbf{r}, \lambda)$ is the product
39 of the light fluence Φ , which itself varies as a function of \mathbf{r} and λ , as well as $\mu_a(\mathbf{r}, \lambda)$ and the
40 reduced scattering coefficient $\mu'_s(\mathbf{r}, \lambda)$:

$$H(\mathbf{r}, \lambda) = \mu_a(\mathbf{r}, \lambda)\Phi[\mathbf{r}, \lambda, \mu_a(\mathbf{r}, \lambda), \mu'_s(\mathbf{r}, \lambda)]. \quad (1)$$

41 This co-dependence of $H(\mathbf{r}, \lambda)$ on both absorption and light fluence leads to an effect known as
42 “spectral coloring”, where variations in local fluence bias the measured optical absorption distribu-
43 tion.^{10,11} Alternative approaches beyond the standard linear unmixing model have been shown to
44 improve $s\text{O}_2$ measurement accuracy, in particular by accounting for the light fluence distribution
45 through: internal irradiation;¹² diffusion theory modelling;^{13–17} Monte Carlo simulations;¹⁸ model-
46 based iterative minimisation;^{19–21} and linear superposition of reference fluence base spectra.²²

47 Several studies have explored ways to validate photoacoustic images using phantoms with well-
48 characterised optical and acoustic properties.^{23,24} Validation of photoacoustically measured $s\text{O}_2$ is
49 possible using CO-oximetry,^{13,25,26} pulse oximetry²⁷ and blood-gas analysis;²⁸ correlation between
50 $p\text{O}_2$ and $s\text{O}_2$ has also been used to study oxygen-hemoglobin binding.²⁹ However, most studies

51 have worked with static blood samples with limited control on the sO_2 . Allowing blood to flow in a
52 circuit^{13,26} and with the ability to vary the sO_2 provides a more versatile platform for investigating
53 PAT oxygenation measurements.

54 In this work, we created a low-cost flow [circuit](#) with online monitoring to facilitate validation
55 of PAT systems. The phantom was tested by circulating different concentrations of methylene blue
56 (MB) and indocyanine green (ICG). The phantom was then applied to explore the accuracy of
57 sO_2 assessment using PAT, with sO_2 values ranging from 0 % to 100 %. We studied the impact of
58 evaluating sO_2 using different reference spectra for HbO_2 and Hb, and also the effect of spectral
59 coloring, showing discrepancies of up to 60 % between the actual and measured sO_2 . Our findings
60 highlight the importance of careful choice of spectra for unmixing and the development of fluence
61 correction models to improve the biological relevance of sO_2 measurements derived from PAT
62 images.

63 **2 Methods**

64 *2.1 Flow system*

65 The flow system (Fig. 1) enables fluids to be circulated within a vessel-mimicking tube embedded
66 in a tissue-mimicking agar phantom placed in the chamber of a photoacoustic imaging system.
67 Online (and offline) flow spectrometry and pO_2 detection provide independent validation of the
68 spectral measurements made by the imaging system. Details of the tissue-mimicking phantom, the
69 photoacoustic imaging system, the spectrometric validation, the pO_2 detection, and the spectral
70 analysis are described in the following subsections.

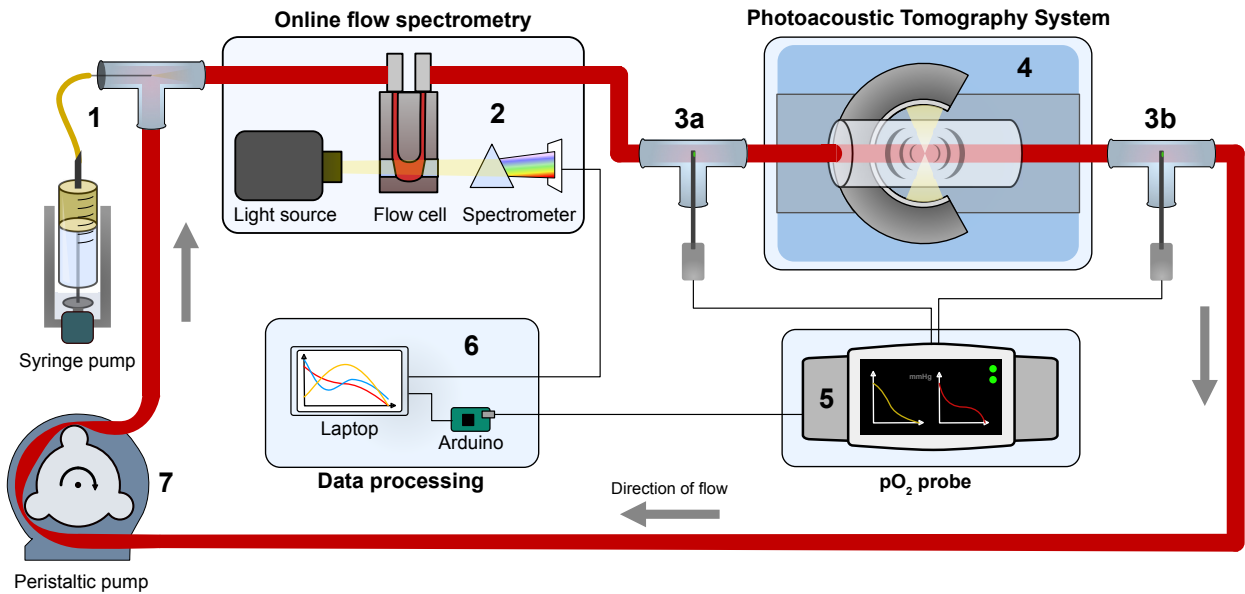


Fig 1 Overview of the flow system. (1) Injection site for introducing oxygenated blood (or other fluids) into the flow system, and for subsequently deoxygenating the blood using sodium hydrosulfite delivered via the syringe driver (MKCB2159V, Harvard); (2) online spectra are recorded using a light source (Avalight-HAL-S-Mini, Avantes) and spectrometer (AvaSpec-ULS2048-USB2-VA-50, Avantes) as the blood passes through a flow cell (170700-0.5-40, Hellma Analytics); (3) needle probes (NX-BF/O/E, Oxford Optronix) measure the temperature and partial pressure of oxygen (pO_2) before (3a) and after (3b) the blood passes through an agar phantom immersed in the photoacoustic imaging system (MSOT inVision 256-TF, iThera Medical) (4); (5) a touch-screen monitor (OxyLite Pro, Oxford Optronix) displays temperature and oxygen data; (6) these data are downloaded via an Arduino UNO and read in MATLAB on a laptop, which also records the spectrometer readings via AvaSoft software; (7) a peristaltic pump (CTP100, Fisher Scientific) provides blood circulation.

71 2.1.1 *Tissue-mimicking phantom*

72 The tissue-mimicking phantom used for photoacoustic imaging comprised either static or flowing
 73 fluids within a tube (“vessel”) embedded within an agar (“tissue”) cylinder, 19 mm in diameter.
 74 Agar phantoms were prepared by heating a solution of 1.5% w/v agar (05039, Fluka) in water, and
 75 then adding 2.1% v/v Intralipid (I141, Sigma-Aldrich), before pouring into an open 20 mL syringe
 76 (with the injection end removed), in the center of which was positioned a needle supporting the
 77 tubing vertically. The solidified agar phantom had a scattering coefficient of 5 cm^{-1} due to the
 78 Intralipid, but the absorption coefficient was assumed to be negligible.

79 To provide optical absorption for assessment of spectral coloring, nigrosin (198285, Sigma-

80 Aldrich) was also added to the tissue-mimicking phantom formulation to produce phantoms with
81 an absorption coefficient of 0.05 cm^{-1} or 0.1 cm^{-1} at 564 nm (the peak of the nigrosin spectrum).

82 *2.1.2 Photoacoustic tomography (PAT)*

83 For photoacoustic imaging, a small animal imaging system (MultiSpectral Optoacoustic Tomog-
84 raphy (MSOT) inVision 256-TF, iThera Medical) was used. Briefly, a tunable optical parametric
85 oscillator (OPO) pumped by an Nd:YAG laser provides excitation pulses with a duration of 9 ns
86 at wavelengths from 660 nm to 1300 nm at a repetition rate of 10 Hz with a wavelength tuning
87 speed of 10 ms and a peak pulse energy of 90 mJ at 720 nm. Ten arms of a fibre bundle provide
88 near-uniform illumination over a disk extending approximately 8 mm along the imaging chamber.
89 Photoacoustic signals are detected using 256 toroidally focused ultrasound transducers with a cen-
90 ter frequency of 5 MHz (60% bandwidth), organized in a concave array of 270° angular coverage
91 and a radius of curvature of 4 cm.

92 *2.1.3 Detection of pO_2*

93 Two oxygen fluorescence quenching needle probes (NX-BF/O/E, Oxford Optronix) were inserted
94 into the flow circuit before and after the tissue-mimicking phantom. A touch-screen monitor
95 (OxyLite Pro, Oxford Optronix) displayed the temperature and partial pressure of oxygen (pO_2)
96 real-time, and these data were downloaded via an Arduino UNO and read in MATLAB. The two
97 measurements before and after the phantom were near-identical, but were recorded so that the
98 mean value could be used to estimate the pO_2 (and temperature) at the photoacoustic imaging site.
99 The relationship between the oxygen saturation (sO_2) and the partial pressure (pO_2) in blood is
100 described by the characteristic sigmoid-shaped oxygen-hemoglobin dissociation curve. A widely

¹⁰¹ accepted fit to this curve is given by the Severinghaus equation:^{30,31}

$$sO_2(\%) = \frac{100}{[23400 \times (pO_2)^3 + 150 \times (pO_2)]^{-1} + 1}, \quad (2)$$

¹⁰² which was used to convert our pO₂ measurements into sO₂.

¹⁰³ *2.1.4 Online flow spectrometry*

¹⁰⁴ Absorption spectra were recorded once per second via AvaSoft software using a light source
¹⁰⁵ (Avalight-HAL-S-Mini, Avantes) and spectrometer (AvaSpec-ULS2048-USB2-VA-50, Avantes)
¹⁰⁶ as the fluid passed through a flow cell (170700-0.5-40, Hellma Analytics).

¹⁰⁷ *2.1.5 Offline spectrometry*

¹⁰⁸ To independently validate spectrophotometric measurements made in the flow circuit, optical ab-
¹⁰⁹ sorbance spectra were also recorded offline using a microplate spectrometer (CLARIOstar, BMG
¹¹⁰ LABTECH). Fluid samples were measured in a 48-well plate (Corning Costar).

¹¹¹ *2.2 Flow system characterization*

¹¹² *2.2.1 Tubing assessment*

¹¹³ The optimum tubing was determined by comparing photoacoustic images obtained of agar phan-
¹¹⁴ toms containing various tube types filled with a 25 µmol ICG solution (Sigma-Aldrich I2633).
¹¹⁵ The tubes were labelled according to their nominal inner and outer diameters (I.D / O.D.) in µm,
¹¹⁶ but were also made of different materials: polypropene 2660/2800 (Alliance Online PSTS0007);
¹¹⁷ THV500 2800/3150, 500/600 (Paradigm Optics); silicone 1570/2410, 630/1190, 300/630 (VWR

₁₁₈ 228-0256, 228-0254, 228-0253); PVC 1500/2100 (VWR 228-3857); PMMA 667/1000, 432/865,

₁₁₉ 375/500 (Paradigm Optics); polythene 580/960 (Smiths Medical 800/100/200 12665497).

₁₂₀ *2.2.2 Dye dilution series*

₁₂₁ A dilution series was used to demonstrate the utility of the flow circuit for injecting different fluids

₁₂₂ into the closed PAT system, allowing PAT to be performed concurrently with online spectrom-

₁₂₃ etry. Methylene blue (MB, 50484, Fluka) and indocyanine green (ICG, I2633, Sigma-Aldrich)

₁₂₄ solutions were prepared by diluting concentrations of 500 µM and 100 µM (for MB and ICG re-

₁₂₅ spectively) in deionized water. First, four spectra were measured and averaged for samples of

₁₂₆ each concentration placed in a 48-well plate in the CLARIOstar spectrophotometer. The concen-

₁₂₇ trations were then flushed individually through the flow system, starting with deionized water and

₁₂₈ then sequentially with increasing concentration. Ten online spectra were recorded over a range of

₁₂₉ 333 nm to 1100 nm, and ten single-slice PA images (no pulse-to-pulse averaging) were acquired

₁₃₀ for 17 wavelengths (660 nm, 664 nm, 680 nm, 684 nm, 694 nm, 700 nm, 708 nm, 715 nm, 730 nm,

₁₃₁ 735 nm, 760 nm, 770 nm, 775 nm, 779 nm, 800 nm, 850 nm, 950 nm), taking the mean of the

₁₃₂ ten single-slice images for each concentration. The circuit was flushed with water between each

₁₃₃ concentration.

₁₃₄ *2.2.3 Dynamic concentration change*

₁₃₅ A dynamic concentration change was used to illustrate the possibility for real-time spectroscopic

₁₃₆ and photoacoustic measurements. Continuous acquisition of online spectra and single-slice pho-

₁₃₇ toacoustic images was commenced once deionized water was circulating within the flow system.

₁₃₈ After a certain time, a high concentration dye solution (either 500 µM MB or 100 µM ICG) was

139 injected using the syringe pump (at 100 $\mu\text{L}/\text{min}$). It was verified that during the estimated few
140 seconds taken for fluid to pass from the online spectrometer to the photoacoustic imaging slice, the
141 changes in the online spectra were insignificant and therefore the acquired spectra could be used
142 to unmix the synchronized photoacoustic images.

143 The amount (moles) of the dye $Q(t)$ in the circuit at any given time t can be modelled using a
144 first order differential equation. In Eq. (3), the rate of change $dQ(t)/dt$ is equal to the difference
145 between the inflow and outflow amounts, expressed in terms of the flow rate F induced by the
146 syringe pump (100 $\mu\text{L}/\text{min}$), the concentration c of dye injected (500 μM or 100 μM) and the
147 volume V (5 mL) of circulating fluid:

$$\frac{dQ(t)}{dt} = F \left[c - \frac{Q(t)}{V} \right]. \quad (3)$$

148 The initial condition is given by Eq. (4), giving rise to Eq. (5), which is the solution for the dye
149 concentration Q/V as a function of time. In the limit $t \rightarrow \infty$, $Q(t)/V \rightarrow c$, as expected.

$$Q(0) = Q_0 = 0; \quad (4)$$

$$\frac{Q(t)}{V} = c \left[1 - e^{-\frac{F}{V}t} \right]. \quad (5)$$

150 *2.3 Blood oxygenation measurements*

151 Mouse blood, predominantly made up of strains B6 and 129SvEv, was collected post mortem
152 from the animal facility at the Cancer Research UK Cambridge Institute, complying with the
153 UK Animals (Scientific Procedures) Act 1986. Each mouse contributed about 1 mL to a pool

154 of approximately 5 mL blood required for the flow circuit. Chemicals were added to preserve,
155 oxygenate and deoxygenate the blood. Prior to the experiment, ethylenediaminetetraacetic acid
156 (EDTA) anti-coagulant (9002-07-7, Sigma-Aldrich) was added to the fresh blood, which was kept
157 in a refrigerator under 4 °C for no more than 72 hours. During the experiment, the blood was re-
158 turned to room temperature, and the oxygenation was controlled chemically by adding 0.2 % v/v
159 hydrogen peroxide, H₂O₂ (7722-84-1, Sigma-Aldrich), for oxygenation³² and sodium hyrosulfite
160 (7775-14-6, ACROS Organics) for deoxygenation.³³ The sodium hyrosulfite was dissolved in
161 phosphate-buffered saline (PBS) ~0.03 % w/v for injection into the flow circuit.

162 *2.4 Spectral and statistical analysis*

163 PAT contrast is provided by optical absorbers within the field of illumination and detection. In gen-
164 eral, PAT does not have sufficient resolution to visualize individual molecules and therefore each
165 image pixel (or voxel) corresponds to more than one optical absorber, and a “spectral unmixing”
166 approach is required in order to extract the individual spectral components. The linear mixture
167 model³⁴ assumes that the measured spectrum is a linear combination of distinct spectra:

$$\mathbf{x} = \mathbf{SC} + n, \quad (6)$$

168 where \mathbf{x} is the M -wavelength \times N -pixels measurement matrix, \mathbf{S} is the $M \times K$ matrix of K spectra
169 (“end-members”), \mathbf{C} is the unknown $K \times N$ matrix of end-member abundances (concentrations),
170 and n is measurement noise. Neglecting n , an estimation $\hat{\mathbf{C}}$ of the absorber concentrations can be

¹⁷¹ calculated from Eq. (6) by solving the following least-squares problem:^{11,35}

$$\hat{\mathbf{C}} = \arg \min_C \|\mathbf{SC} - \mathbf{x}\|_2^2, \quad (7)$$

¹⁷² with the solution

$$\hat{\mathbf{C}} = \mathbf{xS}^+, \quad (8)$$

¹⁷³ where \mathbf{S}^+ is the pseudoinverse of \mathbf{S} . The performance of spectral unmixing carried out on acquired
¹⁷⁴ PA images was compared using three different spectra: those from the literature,^{7–9} and those
¹⁷⁵ experimentally measured in this study from either the online spectrometer cell or the offline plate
¹⁷⁶ reader. In addition, the online flow spectra were used to provide an independent ground truth
¹⁷⁷ for sO_2 ; this entailed unmixing of the online flow spectra with the spectra for oxy- and deoxy-
¹⁷⁸ hemoglobin also measured live during the experiments.

¹⁷⁹ To correct for the spectrally varying fluence (“spectral coloring”) when using optically absorb-
¹⁸⁰ ing phantoms, the image intensities in the tube region were divided by the nigrosin absorption spec-
¹⁸¹ trum. Specifically, the nigrosin absorption spectrum was normalised to the known absorption co-
¹⁸² effient (at the 564 nm absorption maximum) and re-sampled at the 17 experimental wavelengths;
¹⁸³ the multispectral PA data were then divided by a wavelength-specific factor calculated from expo-
¹⁸⁴ nential decay over the 8.5 mm distance from the outer edge of the phantom (the background agar
¹⁸⁵ material impregnated with absorbing nigrosin) to the tube wall. All data and source code used
¹⁸⁶ in this publication is available on <https://doi.org/10.17863/CAM.40365> and GitHub
¹⁸⁷ (<https://github.com/9xg/flow-phantom>).

188 **3 Results**

189 *3.1 Flow system characterization*

190 Eleven different tubes were assessed for their photoacoustic imaging suitability (Fig. 2). Tubes
191 made from PMMA (I.D./O.D. 375/500, 432/865, 667/1000) showed the lowest signal-to-background
192 (SBR) ratios ranging from 0.15 to 0.37. The other tubes materials show a clear trend of increasing
193 SBR with larger inner diameters. Silicone tubes present high SBRs, even for low I.D./O.D. ratios
194 (300/600, 630/1190, 1570/2410). Three PVC tubes showed very similar performance (I.D./O.D.
195 1500/2100, 1570/2410, and 2660/2800). The PVC tube with 1500/2100 presented a uniform, cir-
196 cular appearance in images with high SBR; it was therefore selected for the remaining experiments.
197 Note also that regions of interest (ROIs) indicated on Fig. 2a exclude an outer boundary, but the di-
198 mensions of the image suggest that this boundary is likely to be due to the low frequency response
199 of the detectors rather than absorption by the tube wall itself.

200 Dilutions of MB and ICG were tested inside the flow phantom under closed conditions i.e. with
201 a steady concentration flowing in the circuit. By calculating the mean PA signal intensities over
202 a manually segmented tube cross-sectional region of interest (ROI) for 17 different wavelengths
203 it was possible to compare the PA spectra with those acquired during online flow spectrometry
204 (Fig. 3 (a-d)). Unexpectedly, the two independent spectral measurements show poor agreement in
205 terms of relative intensities and spectral shape for the different dye concentrations. In particular,
206 it is notable that the PA signal intensities (Fig. 3b) show a more pronounced shift in spectral
207 peak with increasing ICG concentration compared with the online spectrometer data (Fig. 3d);
208 this may be a result of spectral coloring where light attenuation at the 800 nm peak suppresses the
209 PA signal intensity deeper within the tube, leading to an overall reduction in mean PA intensity

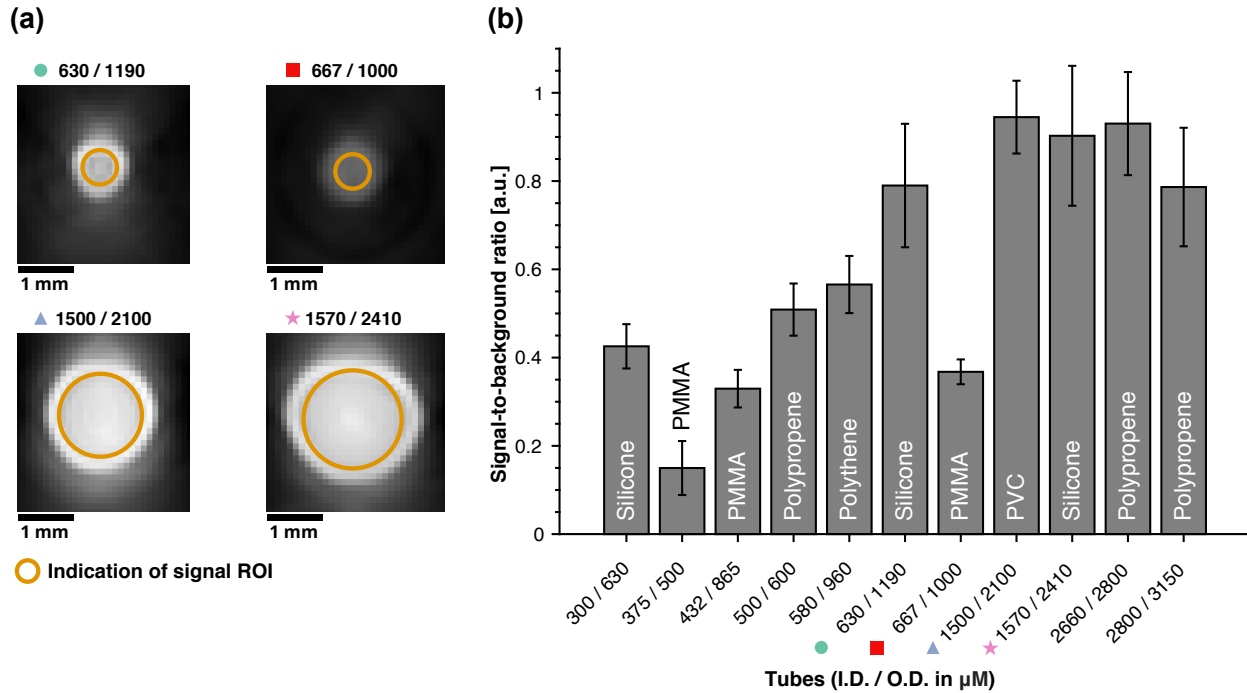


Fig 2 Assessment of the effect of tube type on the quality of photoacoustic images. (a) PAT images (at 775 nm) of four tubes with inner and outer diameters (I.D.-O.D.) in μm of 630-1190 (silicone), 667-1000 (PMMA), 1500-2100 (PVC) and 1570-2410 (silicone), filled with a solution of ICG and embedded within a scattering agar cylinder (not shown). **(b)** Mean photoacoustic signal intensity inside the tube relative to the signal outside (signal-to-background ratio, SBR) for eleven different tubes. The tube with I.D.-O.D. 1500-2100 μm was selected due to its high SBR, flexibility and low cost. The four tubes illustrated in (a) are marked with symbols.

210 at this wavelength. Long fluorescent lifetimes and formation of aggregates are additional factors
 211 that may influence the inversion of the PA spectrum, although they do not explain the absence
 212 of an equivalent spectral shift in the spectrometer data. For MB the discrepancies are difficult to
 213 discern seeing as the prominent spectral features occur below the PA imaging range. However,
 214 it is interesting that the relative PA intensities are about half those for ICG suggesting that MB
 215 has poorer PA signal generation efficiency; this may be related to the long-lived triplet states of
 216 MB, which tend to suppress PA emission and can in fact be exploited in pump-probe techniques to
 217 enhance the PA signal.^{36,37} Overall, these spectral inconsistencies raise a question about which are
 218 the most suitable endmember spectra for unmixing PAT images of MB and ICG.

219 The spectra measured with the online spectrometer and offline in the plate reader were used to

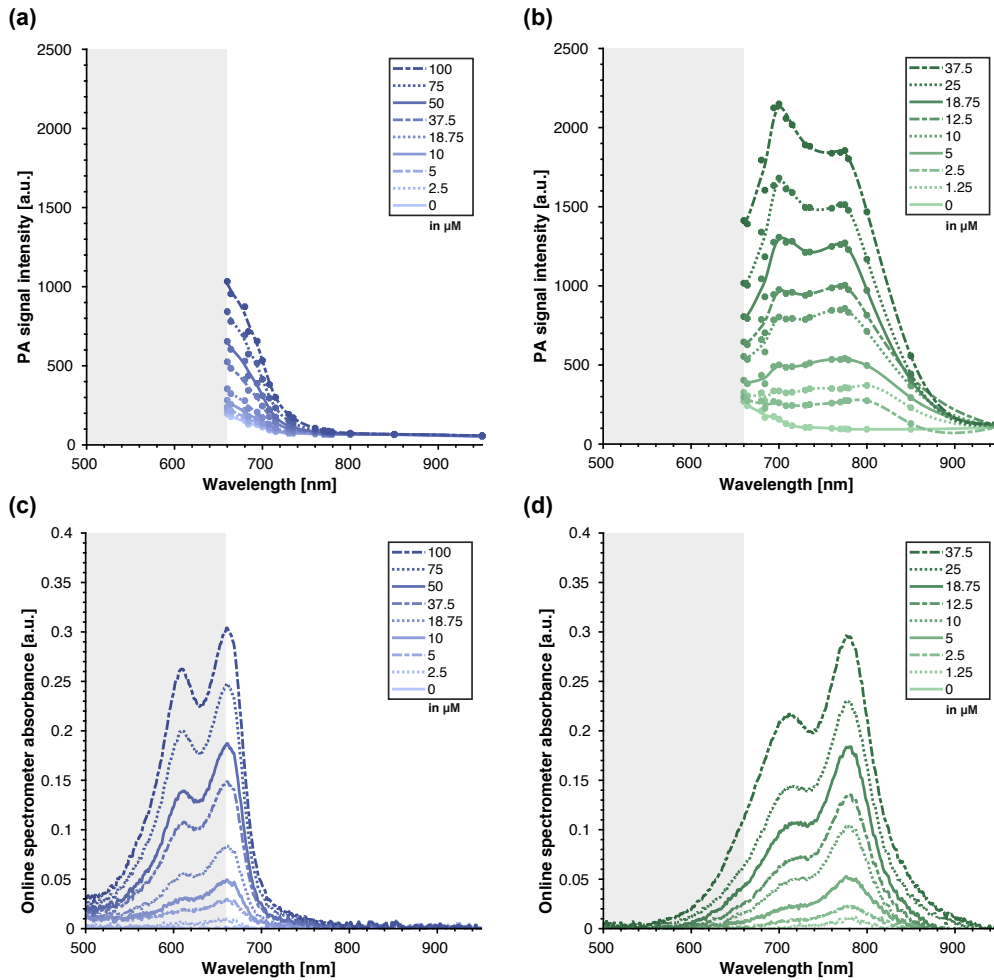


Fig 3 Comparison of dye spectra measured using PAT and online flow spectrometry under closed conditions. (a,b) PA signal intensities (with smoothed spline) and (c,d) online flow spectrometer absorbance values measured for different concentrations of MB (a,c), and ICG (b,d). Grey box indicates wavelengths outside the PAT spectral range.

220 perform concentration-specific unmixing of the mean ROI intensities [recorded at all 17 wavelengths](#),
 221 and these unmixed intensities were compared with those calculated using the literature spectra in-
 222 corporated within the PA analysis software. These literature spectra are shown in Fig. 4 (a-b) along
 223 with online and offline spectra for example concentrations (Fig. 4 (c-f)).

224 Figure 5 (a-b) shows a linear relationship between dye concentration and spectrally unmixed
 225 PA intensities up to $100 \mu\text{mol}$ for MB, and $40 \mu\text{mol}$ for ICG, respectively. Divergence between
 226 the two types of unmixing is likely due to concentration dependent changes in the spectra of these
 227 dyes; these changes are particularly prominent for ICG and indeed the online spectra (Fig. 3d)

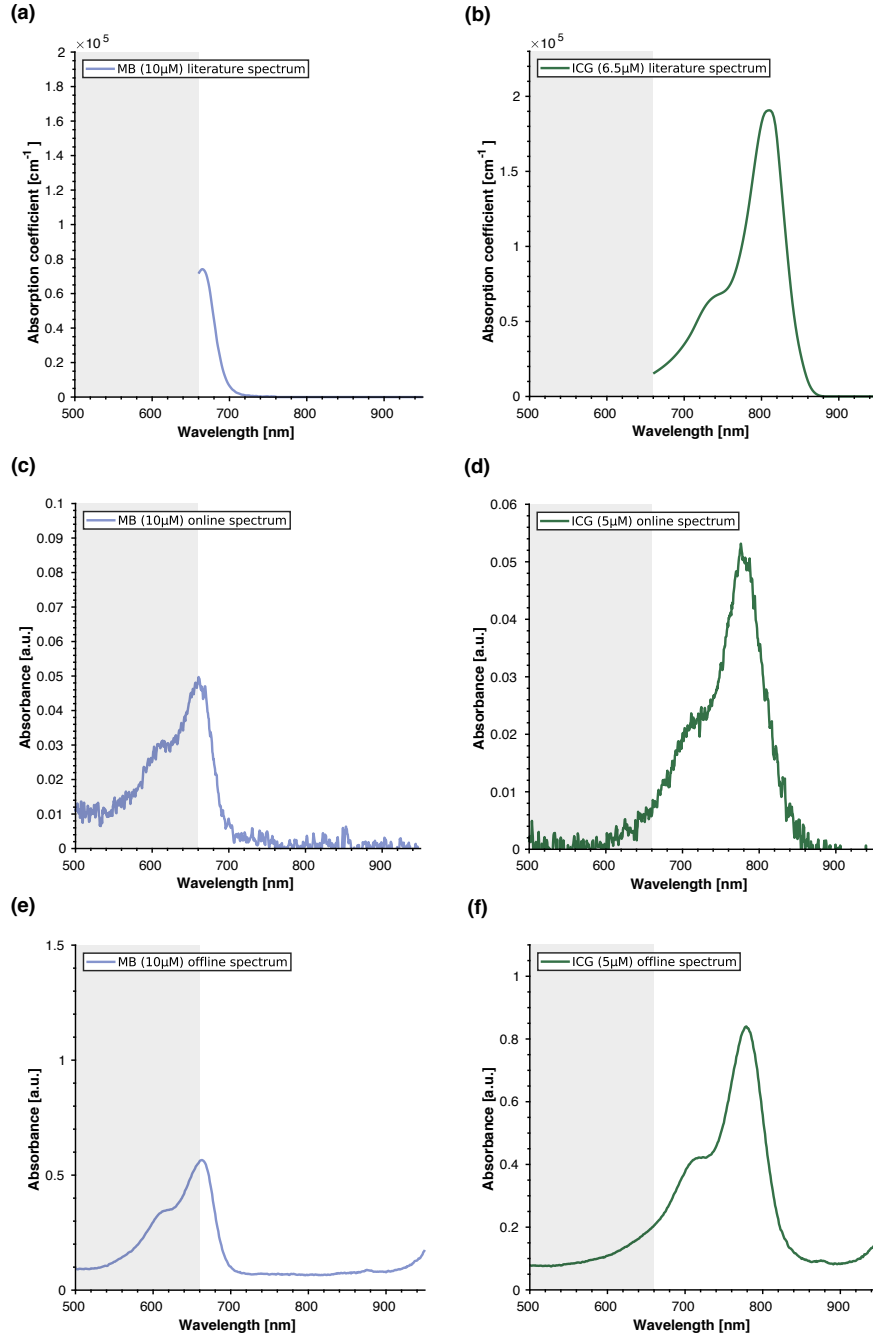


Fig 4 Comparison of endmember spectra used for spectral unmixing. Literature spectra (a,b), spectra acquired using the online flow spectrometer (c,d) and the offline flow spectrometer (e,f) for MB (a,c,e) and ICG (b,d,f).

228 slightly deviate from a linear relationship with increasing concentration.

229 Having explored the application of the flow circuit under static concentration values, we then
 230 examined the response of the PAT instrument to dynamic changes in dye concentrations for MB
 231 and ICG (Fig. 5 (c-d)). PA images were unmixed using the literature spectra and those recorded

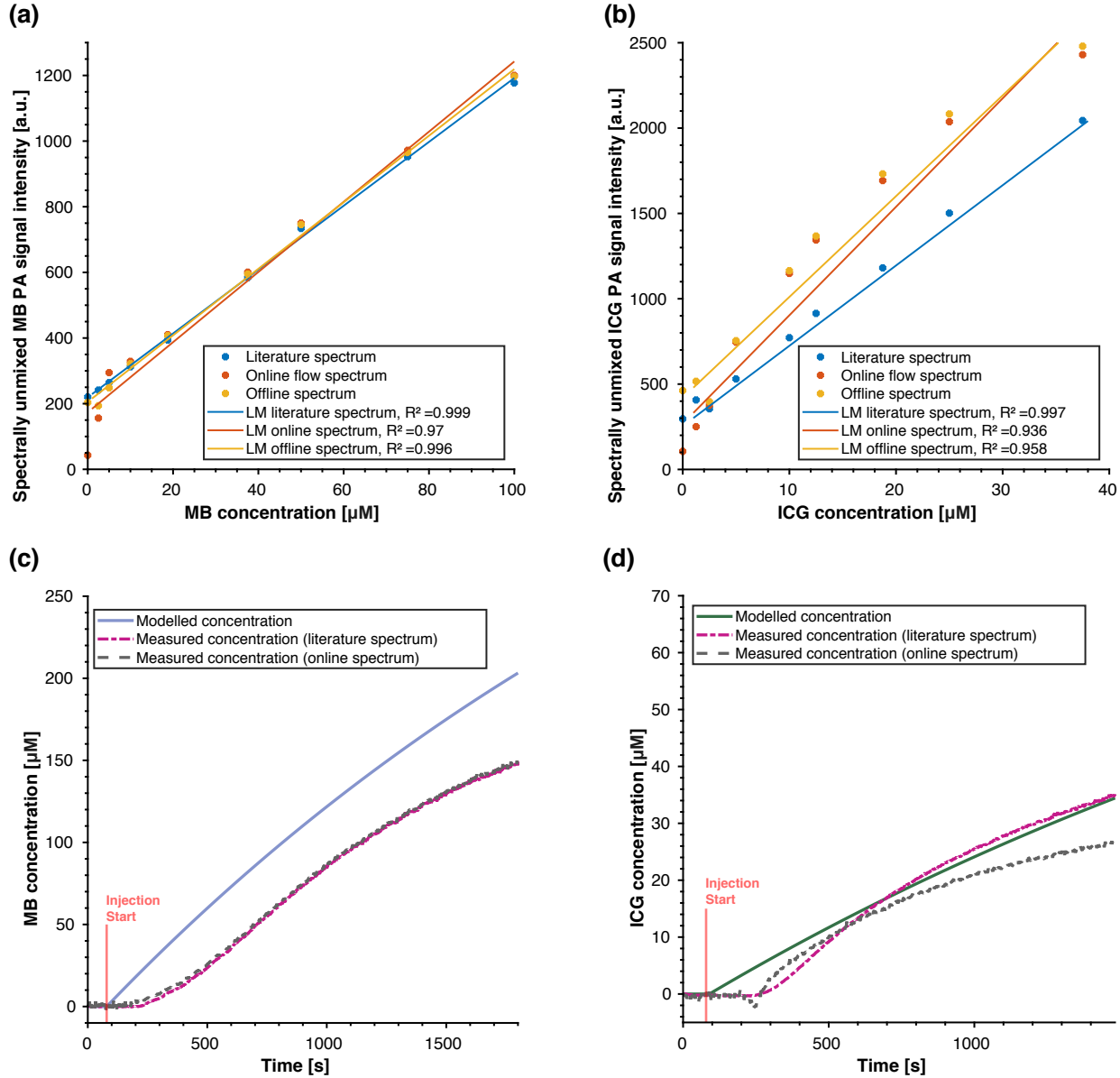


Fig 5 Spectrally unmixed PA signal intensities for a range of dye concentrations. (a) MB and (b) ICG concentrations obtained by unmixing with literature spectra and those measured using the online and offline spectrometers. The linear model (LM) was used to calculate concentrations of MB (c) and ICG (d) during evolution of dye concentrations within the flow circuit due to continual dye injection. The starting points were forced to zero for ease of comparison.

232 live using the online spectrometer, and then converted to absolute concentration values using the
 233 linear models calculated and plotted in (a-b). Neglecting the initial lag phase (which could not
 234 be experimentally determined and therefore was not incorporated into the model), the rates of
 235 concentration change match reasonably well with those predicted by the model (Eq. 5). However,

236 there is a notable discrepancy between the dynamics calculated using the literature and online
237 spectra for ICG unmixing; if the lag phase were corrected for, the online unmixing would be
238 the closer match to the model and this is again likely to be a consequence of the concentration-
239 dependent change in spectral shape, which is incorporated in the online spectra but not the single
240 literature spectrum.

241 *3.2 Blood oxygenation measurements*

242 To demonstrate the closed nature of the blood flow circuit, blood was fully oxygenated by adding
243 approximately 15 μL 0.2 % v/v H_2O_2 to 8 mL mouse blood and then injecting this into the flow
244 system and circulating it for several minutes. Figure 6 shows the blood oxygen saturation (sO_2)
245 measured within the flow circuit by: the pO_2 probe; the online spectrometer and PAT. The sO_2
246 was calculated from the pO_2 data using Equation 2 and from the online spectrometer and PAT data
247 through spectral unmixing. To enable comparison between the methods independently, unmixing
248 was performed using the spectra inherent to each system: for the online spectrometer, experimen-
249 tally measured spectra were used as endmembers, while for PAT data, the literature spectra were
250 used. As hoped, all three sO_2 measurements show consistent values over time. However, the sO_2
251 calculated from the unmixed PA images under-reads by about 13 % compared to the ground truth
252 sO_2 calculated from the pO_2 probe and the online flow spectrometer.

253 In addition to investigating static blood oxygenation within the circuit, the full range of blood
254 sO_2 values (100 % to 0 %) were explored by injecting sodium hydrosulfite into the flow circuit
255 in order to gradually deoxygenate the blood. The blood sO_2 values cover the expected dynamic
256 range when calculated from both the pO_2 probe and the online spectrometer (Fig. 7a); however,
257 PA signal intensities show markedly different behaviors when unmixed with spectra (Fig. 7b)

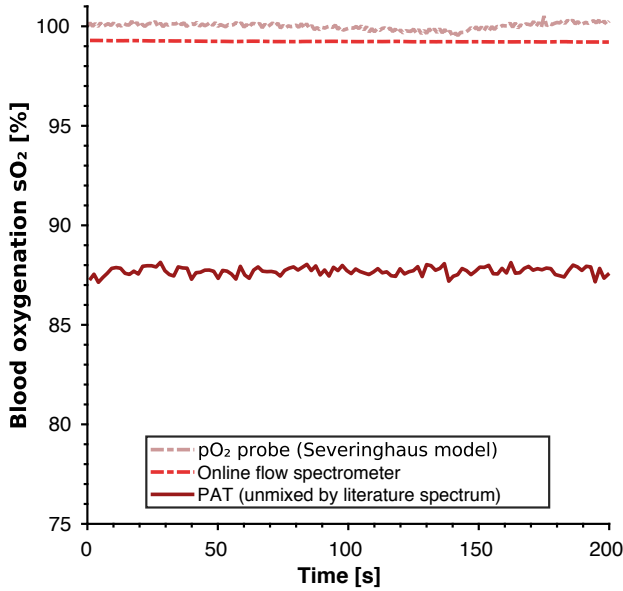


Fig 6 Assessment of blood oxygenation within the flow circuit under closed conditions. Blood oxygen saturation (sO_2) was calculated using the three independent methods: the pO_2 probe measurements (using Equation 2); unmixing of the spectra measured using the online flow spectrometer (with experimentally measured spectra as end-members); unmixing of the mean pixel intensities in the PA images (with literature spectra as end-members) acquired while blood circulated in the flow system for 200 seconds.

from the literature or from the online flow spectrometer. The sO_2 values calculated by unmixing with the experimentally measured spectra (gray dotted line, Fig. 7a) show good agreement with the spectrometer-derived ground truth values (orange/red line, Fig. 7a), except for somewhat over-reading the oxygenation for sO_2 values below about 20 %. They also show a dynamic range comparable to that obtained from the pO_2 probe and Severinghaus model. However, the sO_2 values calculated by unmixing with the literature spectra (pink dashed line, Fig. 7a) surprisingly exhibit a dramatically reduced dynamic range (86 % to 58 %); this may be due to the unmixing spectra and/or spectral coloring.

Two further investigations explored the potential impact of spectral colouring. First, spatially resolved sO_2 measurements were calculated (Fig. 8a). Unlike the results in Fig. 6 and Fig. 7 which were calculated from the mean of the ROI defined on the tube cross-sectional area, the results in Fig. 8a entailed unmixing first using the wavelength-dependent intensities of the single

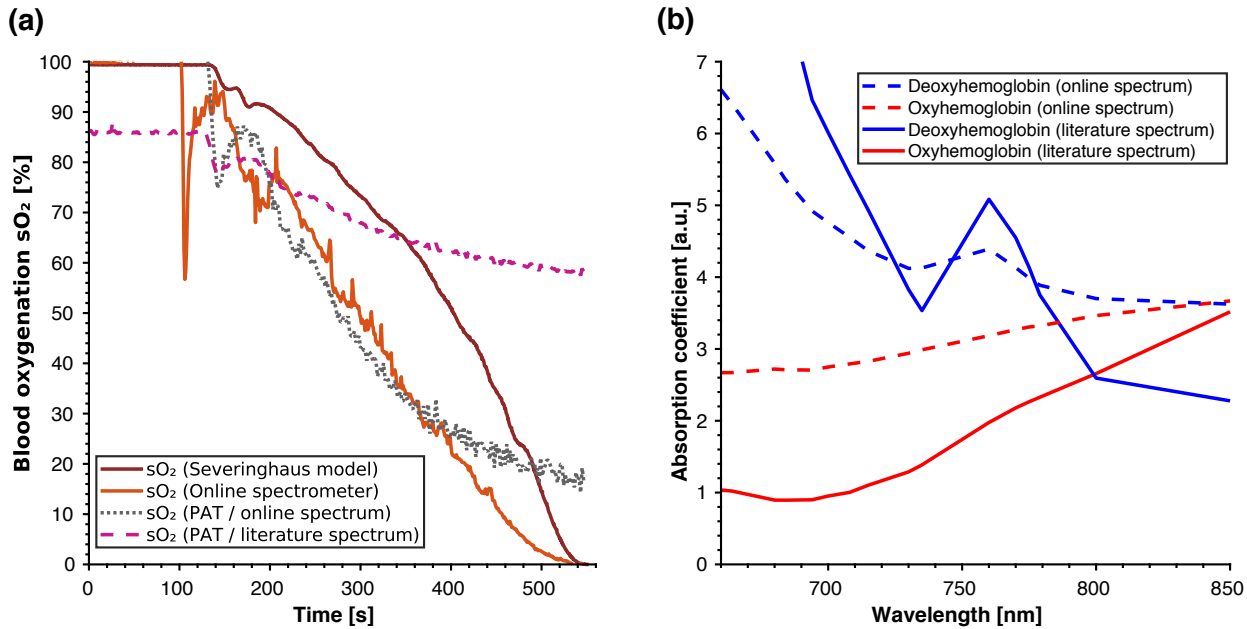


Fig 7 Dynamic deoxygenation of the circulating blood. (a) Change in blood oxygen saturation (sO_2) measured using the pO_2 probe, online spectrometer and PAT system while injecting 3% w/v sodium hydrosulfite in PBS over a period of nine minutes. The anomalous data for the online spectrometer around 100 s may be due to a small bubble passing through the circuit. (b) Literature spectra for oxy- and deoxy- hemoglobin used for spectral unmixing⁷ compared to spectra obtained from the online spectrometer at the start and end of dynamic deoxygenation.

270 pixel at the tube center, and then repeatedly unmixing for the mean intensities of pixels found
 271 in circles increasing in one pixel (75 μ m) increments towards the perimeter of the ROI. For the
 272 fully oxygenated blood the sO_2 values are consistent across the tube diameter, but as the blood
 273 becomes deoxygenated there is a clear trend towards sO_2 over-reading at the center of the tube;
 274 this is a clear demonstration of spectral coloring. A second illustration of spectral coloring is
 275 shown in Fig. 8b where experiments were repeated with absorbing nigrosin dye incorporated into
 276 the background of the tissue mimicking phantom surrounding the flow circuit tube; in all the
 277 previous experiments the agar background was optically scattering but assumed to have negligible
 278 absorption. Increasing the background absorption causes increasing inaccuracy of the sO_2 relative
 279 to the ground truth since wavelengths of light are preferentially absorbed by the nigrosin dye,
 280 leading to over-estimation of the contribution of oxyhemoglobin to the PA signal. A simple light

281 fluence correction, implemented by dividing the images by the known nigrosin spectrum (section
 282 2.4), restored consistent sO_2 measurements irrespective of the background absorption, providing
 283 evidence that this spatial phenomenon is indeed related to spectral coloring.

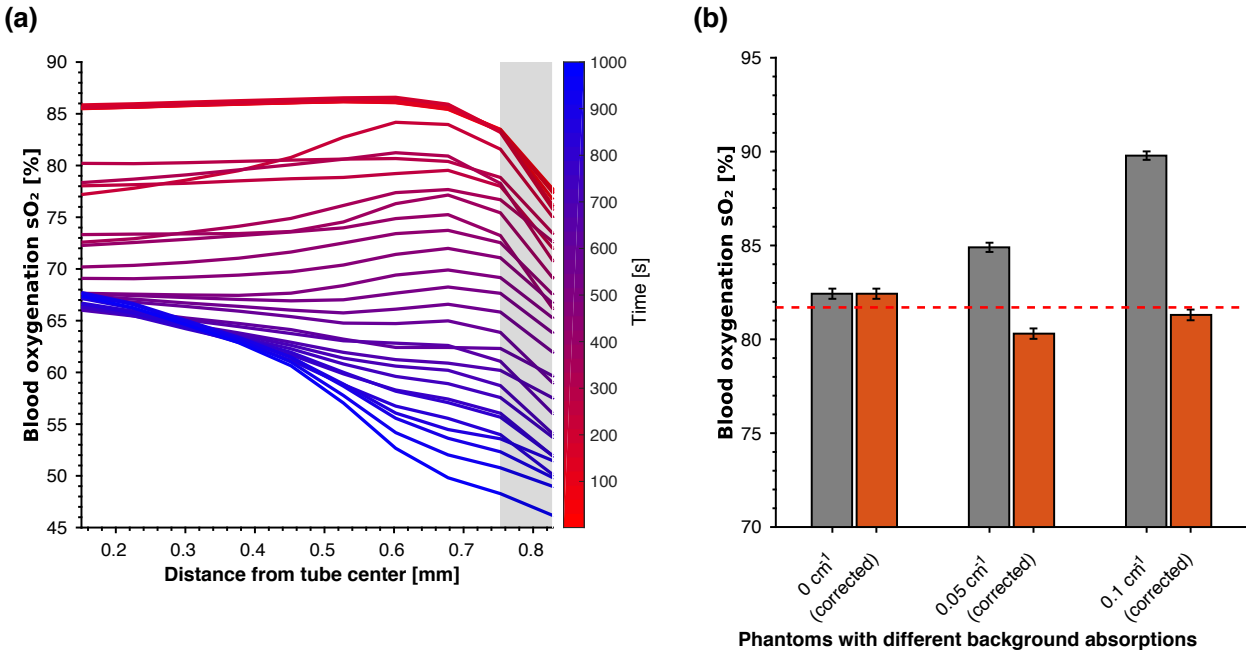


Fig 8 Investigation of spectral coloring. (a) Spatial profiles of blood oxygen saturation (sO_2) as a function of distance from the center of the flow circuit tube by PA unmixing with spectra measured using the online spectrometer during dynamic blood oxygenation (Fig. 7). (b) Impact of correction for the absorption spectrum of the nigrosin dye included in the background of the tissue mimicking phantom as a function of dye concentration. For absorption coefficients of $> 0\text{ cm}^{-1}$ the sO_2 (grey bars) deviated from the ground truth value (dotted line); accurate values were restored by recalculating sO_2 (orange bars) after dividing the photoacoustic images by the relevant nigrosin spectrum as described in the text.

284 4 Discussion

285 The application of PAT in assessment of blood hemoglobin concentration and oxygen saturation is
 286 now widespread, but estimation of the oxy- and deoxy-hemoglobin chromophore concentrations
 287 is affected by a variety of tissue- and instrumentation-dependent factors. We have developed and
 288 applied a low-cost flow phantom system with online monitoring of optical absorption spectra and
 289 partial pressure of oxygen in order to facilitate testing of PAT systems.

290 We first selected an appropriate tubing to maximise PAT image quality and tested the circuit
291 using two optically absorbing dyes. For both dyes, MB and ICG, the absorption spectrum exhibits
292 a double peak where the relative peak intensities shift with increasing concentration. Unmix-
293 ing with a single “average” spectrum is therefore unlikely to yield the same result as unmixing
294 with a concentration-specific (online/offline) spectrum; indeed, we observed different and slightly
295 non-linear relationships between dye concentration and spectrally unmixed intensities (which are
296 assumed to be proportional to concentration) for the two types of unmixing. For ICG, the values
297 from unmixing with the literature spectrum under-read those from unmixing with the online/offline
298 spectra (Fig. 5b,d); for MB the unmixing results were indistinguishable (Fig. 5a,c) since the con-
299 centration dependent effects occur outside of the wavelength range of the PA system under test.
300 It is possible that erroneous concentration measurements may also be caused by spectral coloring,
301 even though only a single component is used in the spectral unmixing; two component unmixing
302 (Hb and HbO₂) is more relevant for calculation of sO₂.

303 We proceeded to evaluate the estimation of sO₂ under both closed circuit and dynamic condi-
304 tions. The results highlight two major factors that contribute to inaccuracies in spectral unmixing,
305 and therefore in sO₂ measurements. The first is the choice of spectra for unmixing the photoacous-
306 tic images; the second is the effect of spectral coloring. The online spectrometer allowed spectra
307 to be recorded during PAT image acquisition and used as alternatives to published spectra for un-
308 mixing the images. Moreover, the ground truth sO₂ values provided by the spectrometer and the
309 pO₂ probes are designed to facilitate exploration of phenomena such as spectral coloring.

310 Images of blood flowing through the circuit entailed unmixing with two components: oxy-
311 and deoxy- hemoglobin. The resulting sO₂ calculations (HbO₂/THb) were consistent over time
312 but were dependent on the hemoglobin spectra used for unmixing, the blood oxygenation satura-

313 tion, and also the position within the tube. The spectra for oxy- and deoxy- hemoglobin measured
314 online were considerably different from those available in the literature that are widely used for
315 spectral unmixing both *in vitro* and *in vivo*. This could be attributed to optical scattering due to the
316 blood cells within the measurement cuvette, as literature studies normally measure the hemoglobin
317 molecule directly. The online flow spectrometer spectra can therefore be described as attenuation
318 spectra, incorporating both absorption and scattering, and using these instead of the literature ab-
319 sorption spectra improved the accuracy of the sO_2 calculations.

320 Over-reading of the lowest sO_2 values was also observed and attributed to spectral coloring:
321 the high absorption by deoxygenated blood at wavelengths below about 750 nm results in low light
322 intensities at these wavelengths in the center of the tube and therefore the PA intensities (propor-
323 tional to both absorption and light fluence) varied with wavelength in a way more closely matching
324 with oxyhemoglobin, leading to overestimation of the oxyhemoglobin concentration. Although
325 this spectral distortion occurring within the tube was not corrected, a simple example of correcting
326 the effects of spectral coloring introduced by the tissue mimicking phantom surrounding the tube
327 was achieved through dividing by the background nigrosin spectrum, which restored accurate sO_2
328 measurements.

329 One limitation of the study is the discrepancy between our measured hemoglobin spectra and
330 those widely used in the literature. Lysing the blood cells would obviate optical scattering and
331 the resulting absorption (rather than attenuation) spectra would therefore be more comparable with
332 those in the literature. Future experiments should also calibrate the measured spectra by extract-
333 ing blood samples from the circuit at different sO_2 values and validating the sO_2 using a blood
334 gas analyser. A further limitation arises from the pO_2 measurements, as the dynamics of the de-
335 oxygenation study did not directly mirror the sO_2 values obtained in the spectrometer. This may

336 be due to an unrepresentative conversion from pO_2 to sO_2 : the Severinghaus equation is derived
337 from human, not mouse, blood data and also assumes certain values for parameters such as pH
338 and temperature. Alternative conversions such as the Kelman equation were also explored, and
339 measured values for pH and temperature were incorporated, but this did not significantly alter the
340 trend in sO_2 over time. It is possible that bubbles or insufficient contact with the blood in the circuit
341 corrupted the pO_2 readings, and therefore future versions of the circuit will integrate truly in-flow
342 pO_2 probes and a membrane oxygenator to avoid bubbles.

343 The application of the presented phantom opens a range of opportunities for future studies of
344 tissue- and instrument-dependent correction factors in PAT. In particular, future work will attempt
345 to model and account for the spectral distortion across the tube diameter observed during blood
346 oxygenation studies. To eliminate the possibility that the tube wall itself contributes to the photoa-
347 coustic signal, future studies will also explore the use of a wall-less phantom. The development
348 of corrections incorporating multiple choromphores inside and outside the tube both *ex vivo* and
349 *in vivo* is more complex and continues to be investigated, for example using Monte Carlo simu-
350 lations and model-based iterative minimisation.^{14,15,17,19–21} Moreover, the number and choice of
351 wavelengths used for spectral unmixing is an important consideration³⁸ to be investigated in future
352 work.

353 5 Conclusion

354 In summary, we have developed a low-cost flow phantom that includes an online spectrometer and
355 partial pressure of oxygen probe to facilitate detailed validation of PAT measurements of blood
356 oxygen saturation, sO_2 . We found that it is important to correctly identify the absorption (or
357 attenuation) spectra to be used for unmixing photoacoustic images in order to accurately determine

358 even relative absorber concentrations. We also found that the co-dependence of photoacoustic
359 signal intensity on light fluence and absorption leads to a major challenge in accounting for spectral
360 coloring, which can lead to substantial underestimation of sO₂. Further calibration and automation
361 of the circuit will enable additional *ex vivo* studies requiring careful control and knowledge of
362 blood sO₂, as well as opening the possibility of exploring additional blood parameters such as
363 pH, and also absorptive and other properties of different fluids. Detailed understanding of the
364 photoacoustic signal origins *ex vivo* remains essential for proper interpretation of photoacoustic
365 measurements made *in vivo*.

366 *Disclosures*

367 SEB has received research support from iThera Medical GmbH and PreXion Inc., vendors of
368 photoacoustic imaging instruments.

369 *Acknowledgments*

370 The authors would like to thank Ayaka Shinozaki for her assistance with data collection, James
371 Joseph for his contributions to the experimental design, and Michael Schneider for his helpful input
372 regarding data interpretation. This work was supported by Cancer Research UK (C47594/A16267,
373 C14303/A17197) and the EPSRC-CRUK Cancer Imaging Centre in Cambridge and Manchester
374 (C197/A16465 and C8742/A18097). We would like to thank the CRUK CI Core Facilities for their
375 support of this work, in particular the Imaging Core and the Biological Resource Unit.

376 *References*

- 377 1 M. Martinho Costa, A. Shah, I. Rivens, *et al.*, “Quantitative photoacoustic imaging study
378 of tumours in vivo: Baseline variations in quantitative measurements,” *Photoacoustics* **13**,
379 53–65 (2019).
- 380 2 I. Quiros-Gonzalez, M. R. Tomaszewski, S. J. Aitken, *et al.*, “Optoacoustics delineates
381 murine breast cancer models displaying angiogenesis and vascular mimicry,” *British Journal
382 of Cancer* **118**, 1098–1106 (2018).
- 383 3 J. Yang, G. Zhang, Q. Li, *et al.*, “Photoacoustic imaging for the evaluation of early tumor
384 response to antivascular treatment,” *Quantitative Imaging in Medicine and Surgery* **9**(2), 160–
385 170 (2019).
- 386 4 M. J. Waldner, F. Knieling, C. Egger, *et al.*, “Multispectral Optoacoustic Tomography in
387 Crohn’s Disease: Noninvasive Imaging of Disease Activity,” *Gastroenterology* **151**(2), 238–
388 240 (2016).
- 389 5 N. Bhutiani, W. E. Grizzle, S. Galandiuk, *et al.*, “Noninvasive Imaging of Colitis Using
390 Multispectral Optoacoustic Tomography,” *Journal of Nuclear Medicine* **58**(6), 1009–1012
391 (2017).
- 392 6 H. F. Zhang, K. Maslov, M. Sivaramakrishnan, *et al.*, “Imaging of hemoglobin oxygen satu-
393 ration variations in single vessels in vivo using photoacoustic microscopy,” *Applied Physics
394 Letters* **90**(5), 053901 (2007).
- 395 7 S. Prahl, *Optical Absorption of Hemoglobin* (1999). <https://omlc.org/spectra/hemoglobin/>.
- 396 8 S. Prahl, *Methylene Blue Spectra* (2017). <https://omlc.org/spectra/mb/>.

- 397 9 M. Landsman, G. Kwant, G. Mook, *et al.*, “Light-absorbing properties, stability, and spectral
398 stabilization of indocyanine green,” *Journal of Applied Physiology* **40**(4), 575–583 (1976).
- 399 10 K. Maslov, H. F. Zhang, and L. V. Wang, “Effects of wavelength-dependent fluence attenua-
400 tion on the noninvasive photoacoustic imaging of hemoglobin oxygen saturation in subcuta-
401 neous vasculature *in vivo*,” *Inverse Problems* **23**, S113–S122 (2007).
- 402 11 B. Cox, J. G. Laufer, S. R. Arridge, *et al.*, “Quantitative spectroscopic photoacoustic imaging:
403 a review,” *Journal of Biomedical Optics* **17**(6), 061202 (2012).
- 404 12 T. Mitcham, H. Taghavi, J. Long, *et al.*, “Photoacoustic-based sO₂ estimation through excised
405 bovine prostate tissue with interstitial light delivery,” *Photoacoustics* **7**, 47–56 (2017).
- 406 13 J. Laufer, C. Elwell, D. Delpy, *et al.*, “In vitro measurements of absolute blood oxygen sat-
407 uration using pulsed near-infrared photoacoustic spectroscopy: accuracy and resolution,”
408 *Physics in Medicine and Biology* **50**, 4409–4428 (2005).
- 409 14 B. Cox, S. Arridge, K. Köstli, *et al.*, “Two-dimensional quantitative photoacoustic image
410 reconstruction of absorption distributions in scattering media by use of a simple iterative
411 method,” *Applied Optics* **45**(8), 4 – 6 (2006).
- 412 15 Z. Yuan and H. Jiang, “Quantitative photoacoustic tomography: Recovery of optical ab-
413 sorption coefficient maps of heterogeneous media,” *Applied Physics Letters* **88**(23), 231101
414 (2006).
- 415 16 J. Laufer, D. Delpy, C. Elwell, *et al.*, “Quantitative spatially resolved measurement of tis-
416 sue chromophore concentrations using photoacoustic spectroscopy: application to the mea-
417 surement of blood oxygenation and haemoglobin concentration,” *Physics in Medicine and*
418 *Biology* **52**, 141–168 (2007).

- 419 17 J. Laufer, B. Cox, E. Zhang, *et al.*, “Quantitative determination of chromophore concen-
420 trations from 2D photoacoustic images using a nonlinear model-based inversion scheme.,”
421 *Applied Optics* **49**, 1219–33 (2010).
- 422 18 Y. Liu, H. Jiang, and Z. Yuan, “Two schemes for quantitative photoacoustic tomography
423 based on Monte Carlo simulation,” *Medical Physics* **43**(7), 3987–3997 (2016).
- 424 19 L. Yao, Y. Sun, and H. Jiang, “Quantitative photoacoustic tomography based on the radiative
425 transfer equation.,” *Optics Letters* **34**, 1765–7 (2009).
- 426 20 F. M. Brochu, J. Brunker, J. Joseph, *et al.*, “Towards Quantitative Evaluation of Tissue Ab-
427 sorption Coefficients Using Light Fluence Correction in Optoacoustic Tomography,” *IEEE*
428 *Transactions on Medical Imaging* **36**, 322–331 (2017).
- 429 21 B. T. Cox, S. R. Arridge, and P. C. Beard, “Estimating chromophore distributions from multi-
430 wavelength photoacoustic images,” *Journal of Optical Society of America A* **26**(2), 443–455
431 (2009).
- 432 22 S. Tzoumas, A. Nunes, I. Olefir, *et al.*, “Eigenspectra optoacoustic tomography achieves
433 quantitative blood oxygenation imaging deep in tissues,” *Nature Communications* **7**(May),
434 12121 (2016).
- 435 23 W. C. Vogt, C. Jia, K. A. Wear, *et al.*, “Biologically relevant photoacoustic imaging phantoms
436 with tunable optical and acoustic properties,” *Journal of Biomedical Optics* **21**(10), 101405
437 (2016).
- 438 24 E. Maneas, W. Xia, O. Ogunlade, *et al.*, “Gel wax-based tissue-mimicking phantoms for
439 multispectral photoacoustic imaging,” *Biomedical Optics Express* **9**(3), 1151 (2018).

- 440 25 R. O. Esenaliev, I. V. Larina, K. V. Larin, *et al.*, “Optoacoustic technique for noninvasive
441 monitoring of blood oxygenation: a feasibility study,” *Applied Optics* **41**(22), 4722 (2002).
- 442 26 W. C. Vogt, X. Zhou, R. Andriani, *et al.*, “Photoacoustic oximetry imaging performance
443 evaluation using dynamic blood flow phantoms with tunable oxygen saturation,” *Biomedical
444 Optics Express* **10**(2), 449 (2019).
- 445 27 S. N. Hennen, W. Xing, Y. B. Shui, *et al.*, “Photoacoustic tomography imaging and estimation
446 of oxygen saturation of hemoglobin in ocular tissue of rabbits,” *Experimental Eye Research*
447 **138**, 153–158 (2015).
- 448 28 Z. Chen, S. Yang, and D. Xing, “In vivo detection of hemoglobin oxygen saturation and car-
449 boxyhemoglobin saturation with multiwavelength photoacoustic microscopy,” *Optics Letters*
450 **37**(16), 3414 (2012).
- 451 29 Y. Wang, S. Hu, K. Maslov, *et al.*, “In vivo integrated photoacoustic and confocal microscopy
452 of hemoglobin oxygen saturation and oxygen partial pressure,” *Optics Letters* **36**(7), 1029
453 (2011).
- 454 30 J. W. Severinghaus, “Simple, accurate equations for human blood O₂ dissociation computa-
455 tions .,” *Journal of Applied Physiology: Re* **46**(3), 599–602 (1979).
- 456 31 J.-A. Collins, A. Rudenski, J. Gibson, *et al.*, “Relating oxygen partial pressure, saturation and
457 content: the haemoglobin-oxygen dissociation curve,” *Breathe* **11**, 194–201 (2015).
- 458 32 D. White and P. Teasdale, “The oxygenation of blood by hydrogen peroxide,” *British Journal
459 of Anaesthesia* **36**, 528–529 (1964).
- 460 33 K. Briely-Sabo and A. Bjornerud, “Accurate de-oxygenation of ex vivo whole blood using
461 sodium dithionite,” *Proc. Intl. Soc. Mag. Reson. Med* **117**(1985), 2025 (2000).

- 462 34 S. Tzoumas, N. Deliolanis, S. Morscher, *et al.*, “Unmixing molecular agents from absorbing
463 tissue in multispectral optoacoustic tomography,” *IEEE Transactions on Medical Imaging*
464 **33**(1), 48–60 (2014).
- 465 35 L. Ding, X. L. Dean-Ben, N. C. Burton, *et al.*, “Constrained Inversion and Spectral Unmix-
466 ing in Multispectral Optoacoustic Tomography,” *IEEE Transactions on Medical Imaging* **36**,
467 1676–1685 (2017).
- 468 36 S. Ashkenazi, “Photoacoustic lifetime imaging of dissolved oxygen using methylene blue,”
469 *Journal of Biomedical Optics* **15**(4), 040501 (2010).
- 470 37 E. Morgounova, Q. Shao, B. J. Hackel, *et al.*, “Photoacoustic lifetime contrast between
471 methylene blue monomers and self-quenched dimers as a model for dual-labeled activatable
472 probes,” *Journal of Biomedical Optics* **18**, 056004 (2013).
- 473 38 R. Hochuli, P. C. Beard, and B. Cox, “Effect of wavelength selection on the accuracy of
474 blood oxygen saturation estimates obtained from photoacoustic images,” in *Proc. of SPIE,*
475 *Photons Plus Ultrasound: Imaging and Sensing*, A. A. Oraevsky and L. V. Wang, Eds., **9323**,
476 93231V–8 (2015).

477 **Marcel Gehrung** completed his MSc degree at Eberhard Karls University Tuebingen in 2017 and
478 is presently completing his PhD in Medical Science at the University of Cambridge focused on the
479 application of advanced image analysis methods for cancer diagnosis.

480 **Sarah Bohndiek** completed her BA degree at the University of Cambridge in 2005 and her PhD in
481 Radiation Physics at University College London in 2008, specialising in X-ray diffraction. After
482 postdoctoral fellowships in both the UK and USA, she started the VISIONLab in Cambridge in

483 2013, which develops and applies new imaging biomarkers to shed light on the tumour microenvi-
484 ronment.

485 **Joanna Brunker** received her MSc degree in natural sciences (2009) and her PhD (2013) in Med-
486 ical Physics and Biomedical Engineering from the University College London, UK. Following her
487 postdoctoral research fellowships at UCL and at the Cancer Research UK Cambridge Institute, she
488 is now (July 2019) starting a research group at the UCL Wellcome / EPSRC Centre for Interven-
489 tional and Surgical Sciences (WEISS) where she will focus on translation of photoacoustic and
490 other imaging technologies into clinical practice.

491 **List of Figures**

492 1 **Overview of the flow system.** (1) Injection site for introducing oxygenated blood
493 (or other fluids) into the flow system, and for subsequently deoxygenating the
494 blood using sodium hydrosulfite delivered via the syringe driver (MKCB2159V,
495 Harvard); (2) online spectra are recorded using a light source (Avalight-HAL-S-
496 Mini, Avantes) and spectrometer (AvaSpec-ULS2048-USB2-VA-50, Avantes) as
497 the blood passes through a flow cell (170700-0.5-40, Hellma Analytics); (3) needle
498 probes (NX-BF/O/E, Oxford Optronix) measure the temperature and partial pres-
499 sure of oxygen (pO_2) before (3a) and after (3b) the blood passes through an agar
500 phantom immersed in the photoacoustic imaging system (MSOT inVision 256-TF,
501 iThera Medical) (4); (5) a touch-screen monitor (OxyLite Pro, Oxford Optronix)
502 displays temperature and oxygen data; (6) these data are downloaded via an Ar-
503 duino UNO and read in MATLAB on a laptop, which also records the spectrometer
504 readings via AvaSoft software; (7) a peristaltic pump (CTP100, Fisher Scientific)
505 provides blood circulation.

506 2 **Assessment of the effect of tube type on the quality of photoacoustic images.**

507 (a) PAT images (at 775 nm) of four tubes with inner and outer diameters (I.D.-O.D.)
508 in μm of 630-1190 (silicone), 667-1000 (PMMA), 1500-2100 (PVC) and 1570-
509 2410 (silicone), filled with a solution of ICG and embedded within a scattering
510 agar cylinder (not shown). (b) Mean photoacoustic signal intensity inside the tube
511 relative to the signal outside (signal-to-background ratio, SBR) for eleven different
512 tubes. The tube with I.D.-O.D. 1500-2100 μm was selected due to its high SBR,
513 flexibility and low cost. The four tubes illustrated in (a) are marked with symbols.

514 3 **Comparison of dye spectra measured using PAT and online flow spectrometry**

515 **under closed conditions.** (a,b) PA signal intensities (with smoothed spline) and
516 (c,d) online flow spectrometer absorbance values measured for different concen-
517 trations of MB (a,c), and ICG (b,d). Grey box indicates wavelengths outside the
518 PAT spectral range.

519 4 **Comparison of endmember spectra used for spectral unmixing.** Literature

520 spectra (a,b), spectra acquired using the online flow spectrometer (c,d) and the
521 offline flow spectrometer (e,f) for MB (a,c,e) and ICG (b,d,f).

522 5 **Spectrally unmixed PA signal intensities for a range of dye concentrations.** (a)

523 MB and (b) ICG concentrations obtained by unmixing with literature spectra and
524 those measured using the online and offline spectrometers. The linear model (LM)
525 was used to calculate concentrations of MB (c) and ICG (d) during evolution of dye
526 concentrations within the flow circuit due to continual dye injection. The starting
527 points were forced to zero for ease of comparison.

- 528 6 **Assessment of blood oxygenation within the flow circuit under closed condi-**
- 529 **tions.** Blood oxygen saturation (sO_2) was calculated using the three independent
- 530 methods: the pO_2 probe measurements (using Equation 2); unmixing of the spec-
- 531 tra measured using the online flow spectrometer (with experimentally measured
- 532 spectra as end-members); unmixing of the mean pixel intensities in the PA images
- 533 (with literature spectra as end-members) acquired while blood circulated in the
- 534 flow system for 200 seconds.
- 535 7 **Dynamic deoxygenation of the circulating blood.** **(a)** Change in blood oxygen
- 536 saturation (sO_2) measured using the pO_2 probe, online spectrometer and PAT sys-
- 537 tem while injecting 3% w/v sodium hydrosulfite in PBS over a period of nine min-
- 538 utes. The anomalous data for the online spectrometer around 100 s may be due
- 539 to a small bubble passing through the circuit. **(b)** Literature spectra for oxy- and
- 540 deoxy- hemoglobin used for spectral unmixing⁷ compared to spectra obtained from
- 541 the online spectrometer at the start and end of dynamic deoxygenation.
- 542 8 **Investigation of spectral coloring.** **(a)** Spatial profiles of blood oxygen satura-
- 543 tion (sO_2) as a function of distance from the center of the flow circuit tube by
- 544 PA unmixing with spectra measured using the online spectrometer during dynamic
- 545 blood oxygenation (Fig. 7). **(b)** Impact of correction for the absorption spectrum
- 546 of the nigrosin dye included in the background of the tissue mimicking phantom as
- 547 a function of dye concentration. For absorption coefficients of $> 0 \text{ cm}^{-1}$ the sO_2
- 548 (grey bars) deviated from the ground truth value (dotted line); accurate values were
- 549 restored by recalculating sO_2 (orange bars) after dividing the photoacoustic images
- 550 by the relevant nigrosin spectrum as described in the text.